Eur. Phys. J. Plus (2019) **134**: 596
DOI 10.1140/epjp/i2019-12946-9

THE EUROPEAN PHYSICAL JOURNAL PLUS

Regular Article

Pore-scale numerical modeling of coupled fluid flow and medium geometrical deformations in an unconsolidated porous medium

Behnam Nasrollahzadeh[1], Hossein Ali Akhlaghi Amiri[1,a], and Siavash Ghabezloo[2]

[1] Department of Chemical Engineering, Faculty of Engineering, Ferdowsi University of Mashhad, Mashhad, Iran
[2] Laboratoire Navier, Ecole des Ponts ParisTech, Ifsttar, CNRS UMR 8205, Marne-la-Vallée, France

Received: 10 May 2019
Published online: 4 December 2019

Abstract. The interplay of fluid flow and medium grains' deformation/movement in unconsolidated porous media was numerically studied. The numerical simulations were done through coupling Cahn-Hilliard phase field and Navier-Stokes equations for fluid flow as well as stress-strain and Arbitrary Lagrangian/Eulerian mesh alteration equations for geomechanical effects, by the finite-element method. Single/two-phase flow through a real patterned micro-scale medium with/without grains' deformation and movements/rotation were studied. In single-phase models, the fluid velocity distribution was quite similar for the cases with rigid grains and that with only deformed grains. However, in an unconsolidated medium, the velocity magnitude and distribution were modified. The medium porosity had a linear trend with pressure, and was independent of the grains' movement/rotation. The models with deformed grains showed good agreement with Kozeny-Carman equation in permeability variation *versus* pressure. In the two-phase flow models, the velocity/displacement profiles, relative permeability end-points and capillary pressure were quantitatively compared in rigid and unconsolidated media *versus* medium wettability. The effect of the grains' deformation on the fluid distributions was negligible at low capillary numbers, especially in water-wet and neutral wetting conditions. However, the grains' movement/rotation considerably modified the flow regime at different grains' contact angles. At higher capillary numbers, the grains' deformation effect was more pronounced.

1 Introduction

Single- and multi-phase displacements in porous media have wide applications in a variety of subsurface fields such as underground water streams, contamination transports, recovery of hydrocarbon —including oil and gas— reservoirs and CO_2 sequestrations [1]. During the last decades, numerous experimental and numerical works have been reported, which studied such phenomena [2–12]. Fluids' properties, interfacial tension, medium pore structures and surface wettability have been found as the main effective parameters on displacement characteristics [13–16]. The geomechanical behavior of porous media, on the other hand, could be another effective parameter which may indirectly influence the fluid flow by modification of the pore structures [17]. Deformation and movements of the rock grains under stresses, caused by fluids' pressure and velocity, may considerably change pore-scale flow properties and displacement patterns [18,19].

Geomechanical studies have been frequently addressed in fluid flow problems through porous media at field-scales [20–29]. Also, it is possible to find numerous works at the macro-scale, both experimentally and numerically, which studied the interaction of the medium deformation and fluid flow in rock core samples and sand-packs. Some of those [30–35] used finite element modelling to simulate the reservoir rock core samples under fluid flow, investigating the temporal and spatial variations of the fluid pressures inside the deformable porous media. Xikui *et al.* [31,32] studied the two-phase (water and oil) flow and defined an appropriate formulation for pore pressure which could better simulate the variation of pore pressure and displacements in the medium. Rahman *et al.* [33] presented a multiphase flow model (gas, water and nonaqueous phase liquid) and observed that vertical displacement as well as water saturation in porous media could be predicted by their model, in agreement with the experimental data. Coupled

[a] e-mail: ha.akhlaghi@um.ac.ir

Lattice Boltzmann and finite-elements formulation was used by White *et al.* [34,35] to simulate the flow inside a sand-pack. They showed that both compaction and pressure fields were in correspondence with 3D microtomographic images of the studied sand-pack. Fattahi *et al.* [36] used the distinct element method (DEM) in a domain of circular particles and concluded that the interaction of fluid flow and reservoir rock displacements was more significant in a hydraulic fractured reservoir in comparison to a naturally fractured one. A coupled model of fluid flow and DEM was developed by Boutt *et al.* [37] and Bakhshian *et al.* [38] to study the flow in the sand-pack samples. They showed that for correlating the permeability with the porosity, the Kozeny-Carman shape factor depends on porosity and would be predicted in a purely empirical manner. Pan *et al.* [39,40] used the volume-averaging technique and showed that pore structure parameters, such as initial porosity and averaged channel width, resulted in different matrix displacements. Both *et al.* [41] proposed a new linearization scheme and compared its robustness and convergence with the classical Newton's method. The homogenization theory of periodic structures was developed by Auriault *et al.* [42]. They showed that the determined physical stress was in better agreement with the experimental results, compared to the volume averaged stress formulation. Ju *et al.* [43] observed that the consideration of both rock and fluid compressibilities besides the pressure-dependent viscosity of the fluid resulted in a more precise prediction compared to the model treating these parameters as constants [43]. Hewitt *et al.* [19] showed that if a deformable medium was taken into account, the fluid flux would not increase linearly with the pressure head, as observed in classical rigid media. Instead, the flux would raise toward a limited maximum as the pressure increased.

It is well known that the macroscopic phenomena during the fluid flow in porous media may remain unpredictable as long as the pore-level physics of the events is not deeply understood [37,44–47]. However, one can rarely find pore-scale studies on the interaction of geomechanics and fluid flow through porous media; and in the few reported experimental and numerical works, porous media with simple geometries have been studied. Torrealba *et al.* [48] conducted pore-scale experiments on the two-phase flow through bead packs, with spherical shapes, under different pressures. The X-ray micro-CT method was used to observe the extent of the medium deformation and the fluid distributions. Increasing the capillary number resulted in higher pore contraction and pore fluid velocity. An experimental study was done by Kaneko *et al.* [49] on the collapse of cavity regions and their interactions in a homogenous glass bead, caused by a viscous fluid flow. The results demonstrated that at a specific terminal velocity, grains were moved from a boundary to another one. Similar studies were done by Siddique *et al.* [50] on spherical glass beads. They concluded that gravity results in capillary suction of fluid to the pores and consequent solid deformation. Chekired *et al.* [51] performed DEM simulation of creeping single-phase flow in a system of deformable 2D circular soil particles. Their model could capture transport and deposition rates of the particles in erosion phenomena under fluid flow. Similar study by Hellstrom *et al.* [17] showed that a more compact system of equal-sized particles results in a higher probability of changes in permeability at higher fluid flow rates. Prodanović *et al.* [18] worked on dynamics of 3D sphere-packs in response to increased capillary pressure during immiscible gas/water displacements. They observed that movability of grains had a significant effect on the nature of the gas/water drainage displacement.

In this work, single- and two-phase displacements were numerically simulated using the finite-element method, through a 2D real patterned heterogeneous porous medium with complex geometry; contrary to the above referenced studies, in which the grains had simple geometries, *e.g.*, spheres and circles. In the simulated models, the coupled effects of fluid flow and the medium grain's mechanical behaviors were addressed at pore-scale. In the single-phase flow model, the effects of the medium pressure, injection velocity, and fluid viscosity are quantified on the grain's deformation/movements, medium porosity and permeability, as well as the resultant fluid velocity distribution in the medium. In the two-phase flow models, the interacting effects of the fluid displacements and the medium geomechanical behavior are studied under different capillary numbers at various medium wettability conditions. The capillary pressure distribution and the relative permeability endpoints were compared in two-phase simulated media.

2 Theory and numerical methods

In this section, the theoretical framework of the performed simulations are described. Also, the applied numerical simulation method is presented.

2.1 Two-phase flow equations

The Cahn-Hilliard phase-field method [52] was coupled with Navier-Stokes and continuity equations to solve the interfacial problems. The fluids are supposed to be Newtonian, incompressible and immiscible, with constant physical properties and without phase change. In the phase-field method, an order parameter (ϕ) is defined such that $\phi = \pm 1$ represents the bulks of the two phases and $-1 < \phi < 1$ represents the interface. The relative concentrations of the two components are then $\frac{1+\phi}{2}$ and $\frac{1-\phi}{2}$. All the fluid physical properties are interpolated between the two phases using the relative concentrations of the phases [5,7]:

$$\pi(\phi) = \frac{(1+\phi)}{2}\pi_1 + \frac{(1-\phi)}{2}\pi_2, \tag{1}$$

where π denotes phase properties such as viscosity (μ) and density (ρ). The phase-field equation is then coupled with the modified Navier-Stokes and continuity equations to represent the moving interface. In this study gravity is neglected, assuming 2D horizontal flow, so the equation system for the two-phase flow simulation is as follows [5,7]:

$$\rho\frac{\partial \boldsymbol{V}}{\partial t} + \rho(\boldsymbol{V}\cdot\nabla)\boldsymbol{V} = -\nabla p + \nabla\cdot[\mu(\nabla\boldsymbol{V} + \nabla\boldsymbol{V}^T)] + G\nabla\phi, \tag{2}$$

$$\nabla\cdot\boldsymbol{V} = 0, \tag{3}$$

$$\frac{\partial\phi}{\partial t} + \boldsymbol{V}\cdot\nabla\phi = \nabla\cdot\left(\frac{\chi\lambda}{\epsilon^2}\right)\nabla\psi, \tag{4}$$

$$\psi = -\nabla\cdot\epsilon^2\nabla\phi + (\phi^2-1)\phi, \tag{5}$$

where p denotes the fluid pressure, $\boldsymbol{V}$ is the fluid velocity field and t is the time. ψ is an auxiliary parameter, which decomposes the fourth-order Cahn-Hilliard equation to two second-order equations ϵ is the interface thickness parameter, χ is the mobility, λ is the mixing energy density, and G is the chemical potential which is defined as $G = \lambda[-\nabla^2\phi + \frac{\phi(\phi^2-1)}{\epsilon^2}]$. In this model, the mixing energy (f_{mix}) is obtained by the well-known Ginzburg-Landau formulation as follows [53,54]:

$$f_{mix}(\phi,\nabla\phi) = \frac{1}{2}\lambda|\nabla\phi|^2 + \frac{\lambda}{4\epsilon^2}(\phi^2-1)^2. \tag{6}$$

The surface tension is considered here as an intrinsic property and is defined as $\gamma = \frac{2\sqrt{2}\lambda}{3\epsilon}$ [53].

Other details about phase-field theory and formulation can be found in [53–57].

The governing equations are completed by standard boundary conditions (*e.g.*, inlet, outlet, no-slip, wetted wall and symmetry). On the solid wetted grains, the following boundary conditions are implemented:

$$\boldsymbol{V} = \boldsymbol{V}^s, \tag{7}$$

$$n\cdot\epsilon^2\nabla\phi = \epsilon^2\cos(\theta)|\nabla\phi|, \tag{8}$$

$$n\cdot\left(\frac{\chi\lambda}{\epsilon^2}\right)\triangle\,\psi = 0, \tag{9}$$

where n is the unit normal to the wall and θ is the surface contact angle. $\boldsymbol{V}^s$ is the grains' movement velocity, which is described more in the next sect. $\boldsymbol{V}^s$ is zero in the rigid media and is nonzero in the case of the grains' movement. The details about other boundary equations can be found in [53,54].

2.2 Grain's deformation and movement equations

The medium grains are considered as solid linear elastic materials with homogeneous and isotropic properties. Further, the chemical effects between the fluids and the grains were neglected.

The system of equations for describing the deformation of solid objects included by the balance of forces exerted on the rock grains solid body [58], stress-strain and strain-deformation relations is as follows:

$$-\nabla\cdot\sigma = \int p\,\mathrm{d}A, \tag{10}$$

$$\varepsilon_{ij} = \frac{1}{E}[(1+\nu)\sigma_{ij} - \nu\delta_{ij}\sigma_{kk}], \tag{11}$$

$$\varepsilon = \nabla d, \tag{12}$$

where σ, ε and d are the stress, strain and deformation tensors, respectively. i, j and k are the space directions of the strain and stress tensor elements. E is Young's modulus, ν is Poisson's ratio and δ_{ij} is the Kronecker delta matrix. Equation (11) is the linear elastic constitutive equation, known as Hook's law, for an isotropic and homogeneous solid material, relating the stresses and strains variables [58]. Equation (12) relates the strains and deformations assuming solid's irrotational deformation [59]. Solving the system of equations (10) to (12) simultaneously results in stress, strain and deformation variables of the rock grains.

The total drag which is exerted from the fluid on the boundaries of the solid body, resulting from normal and shear stresses, is calculated by [60]

$$\boldsymbol{f} = \mathbf{n}\cdot\left\{-p\mathbf{I} + (\mu(\nabla\boldsymbol{V} + (\nabla\boldsymbol{V})^T) - \frac{2}{3}\mu(\nabla\cdot\boldsymbol{V})\mathbf{I})\right\}, \tag{13}$$

where $\mathbf{n}$ and $\mathbf{I}$ represent the normal boundary vector, and identity matrix, respectively. Movement of the rock grains is then described by eq. (14), derived from Newton's second law:

$$\boldsymbol{F} + \boldsymbol{k} \cdot \boldsymbol{u} = m\frac{\mathrm{d}\boldsymbol{V}^s}{\mathrm{d}t}\,, \qquad \boldsymbol{V}^s = \frac{\mathrm{d}\boldsymbol{u}}{\mathrm{d}t}\,, \tag{14}$$

where $\boldsymbol{F}$ represents the forces exerted on the rock grains solid body, calculated by integrating the components x and y of parameter f on the surface of each particle from eq. (13). $\boldsymbol{u}$ is the movement vector which associates the position of a rock grain in the basic structure to its new position in the new structure. m is the average mass of the rock grain. $\boldsymbol{k}$ is the total spring constant for consideration of the spring force exerted on each grain to take into account the properties of the cement material in a real reservoir among grains and lack of free movability for grains inside the porous medium. Further, in the simulations, to prevent collision of the grains, it has been assumed that the rock grains inside the domain of the porous medium do not approach each other by more than 10% of the average grains' diameter.

Eventually, fluid flow and grains' displacement equations need to be coupled in a system of equations in order to calculate the extent of rock deformation and movement as well as the velocity and distribution profile of fluids. The pressure and velocity distribution of fluids in the fluid domain are calculated by eq. (2) and inserted in eq. (13) to calculate the net fluid stress exerted by the fluids on the surface of each grain. Subsequently, the x and y components of parameter $\boldsymbol{F}$ in eq. (14) are described. Also, the force load on the boundary of each grain for the deformation of the solid body is calculated by the right-hand side of eq. (10). The boundary condition of grains in the fluid flow model is considered as a moving boundary, calculated by eq. (14) in which velocity and acceleration of grains' movement are described by Newton's second law.

2.3 Numerical methods

The numerical simulations have been performed using the COMSOL Multiphysics$^{\mathrm{TM}}$ (2013) software, which has an interactive interface for modeling different engineering and scientific problems. This software uses the finite-element method to solve the partial differential equations. It also runs the finite-element analysis alongside the error control using various numerical solvers [61].

In this study, triangular mesh elements have been used across all calculations. The arbitrary Lagrangian and Eulerian (ALE) method has been used for alternation in the mesh in the numerical simulation of a fluid flow in a deformable and moveable porous medium of grains. In this method, when the mesh displacement is equal to the velocity of the deformed porous medium, the term of displacement which represents the relative velocity between the fluid flow and the deformed porous medium is omitted from finite-element method calculations. Therefore, part of the challenges in simulation by the FEM is resolved [62]. Further details of the ALE concept are presented in Haughes *et al.* and Liu *et al.* [63,64]. To ensure the accuracy of the results and prevent nonphysical distortion of meshes and thus the development of error in the two-phase fluid flow calculations, the interface region should be adequately solved by fine mesh. These conditions have been described in detail in the paper by Zhu *et al.* [54], who have examined the convergence of the model and convergence of mesh. In PFM, mobility is another important parameter that affects the accuracy of the method [55]. Selection of the mobility parameter (χ) is one of the intricacies of the PFM. χ should be large enough to keep the interface thickness constant, and small enough to keep the convective motion [53]. Sensitivity analysis studies by Akhlaghi Amiri and Hamouda [5] suggest that simulation with $0.1 < \chi < 1$ causes less volumetric contraction of fluids in the simulation of two-phase fluid problems. Thus, $\chi = 1$ is used in the present study.

As discussed by Yu *et al.* [53], to apply finite element discretization, the fourth derivative term in eq. (4) should be divided by two second order equations using an auxiliary parameter. Therefore, PFM calculations are performed by four dependent variables $\{\boldsymbol{V}, p, \phi, \chi\}$. Moreover, coupling PFM calculations with rock grains' deformation and movement equation lead to calculate the unknown variables of fluids model besides the solid mechanics model $\{\boldsymbol{V}, p, \phi, \chi, \sigma, \varepsilon, \boldsymbol{u}, d\}$. Further, in this study discretization of the domain is performed by a uniform mesh sizes of $2\,\mu$m. Although it causes increased computational cost, it offers problem convergence and numerical accuracy of the results. Considering the mean diameter of pores in the porous medium as the characteristic length (l_c) and based on the definition of Cahn number as $Cn = \epsilon/l_c$, as specified in the work by Akhlaghi Amiri and Hamouda [5], use of $Cn = 0.03$ and a mesh size $h = 0.8\epsilon$ results in both model and mesh convergence for the phase field method.

The size of time steps along calculations is controlled by numerical solver using backward differentiation formulas (BDFs). The initial time steps size is selected small enough in order to prevent development of singular matrix. The equations of interface displacement in the two-phase fluid flow should be initialized before the time-dependent solution. In the initialization stage, the interface is solved under steady conditions ($\boldsymbol{V} = 0$), so that ϕ changes gradually along the initial interface.

3 Results and discussion

First, the constructed simulation method, which includes equations of fluid flow and grain's solid mechanics, is validated with the analytical solution of a simple model. Then, this method is used for pore-scale simulating the interplay of

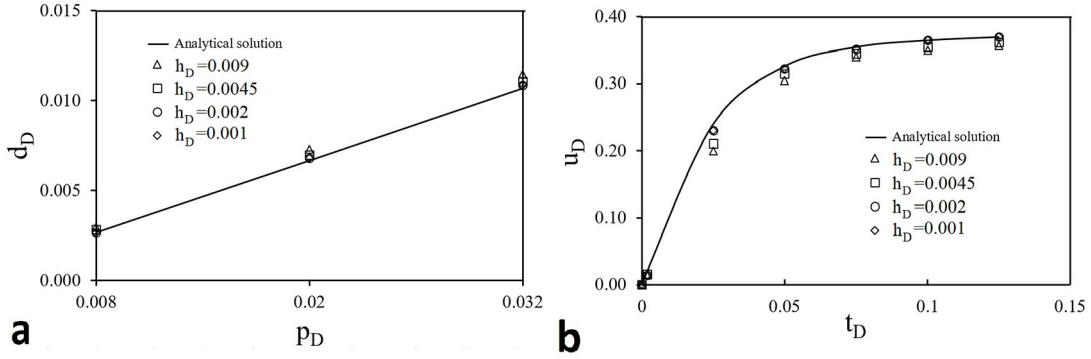

Fig. 1. Comparison of analytical solution and numerical simulation results of (a) dimensionless radial grain deformation (d_D) as a function of dimensionless pressure (p_D), and (b) dimensionless grain displacement (u_D) *versus* dimensionless time (t_D), at different mesh element sizes.

geomechanics and single/two-phase flow in an unconsolidated real patterned porous medium. The effects of different parameters, such as fluid pressure, viscosity and injection rate as well as the medium wettability on the grain's deformation/movement and fluid displacements are then evaluated.

3.1 Model validation

A simple model is used for validation, which involves a circular solid grain, with diameter (D_g) of 1 mm, Poisson's ratio (v) of 0.2, and Young's modulus (E) of 2500 MPa, placed through a horizontal 1D single-phase (water) flow with constant velocity (V_i) of 5×10^{-6} m/s. Simulations at different fluid pressures (p) of 0, 20, 50 and 80 MPa were performed. This model was solved numerically, at different mesh element sizes, and the results were compared with the analytical solutions (fig. 1), obtained by analytical solution of ordinary differential equations discussed previously for this simple problem. Figure 1(a) compares the numerically and analytically obtained dimensionless radial deformation of the grain, $d_D = \frac{d}{D_g}$, at different dimensionless pressures, $p_D = \frac{p}{E}$. The domain was discretized with mesh elements at different dimensionless sizes ($h_D = \frac{h}{D_g}$). The grain deformed linearly with confining fluid pressure and numerical model accurately predicted this deformation trend, especially at $h_D \leq 0.002$. Figure 1(b) shows the obtained results of numerical and analytical grain dimensionless displacement ($u_D = \frac{u}{D_g}$) *versus* dimensionless time ($t_D = \frac{tV_i}{D_g}$) at zero fluid pressure. The grain movement had an initial acceleration, due to the pressure and viscous drag, then experienced almost a constant velocity (linear trend in fig. 1(b)) which was gradually damped by the employed spring effect. It was finally almost stopped after about $t_D = 0.1$. The numerically obtained trend for the grain displacement is in good agreement with the analytical result at $h_D \leq 0.002$.

The constructed coupled phase field and Navier-Stokes model was previously verified using extensive numerical sensitivity studies [5] and was carefully validated with analytical solution of Poiseuille two-phase flow inside a channel [5, 7] as well as micro-scale experimental observations in a wide range of capillary-viscous governing displacements [7,65]. The results indicated great accuracy, and confirmed the ability of such a model in the prediction of the two-phase flow behavior at different fluid/medium conditions in media with complicated pore morphologies.

3.2 Single-phase flow models

The geometry of the studied porous medium (fig. 2) is based on the Scanning Electron Microscopic (SEM) image of a real medium described by Keller *et al.* [66]. In fig. 2, the medium grains are presented with dark color and the flow inlet and outlet boundaries are specified with arrows. The characteristics of the simulated medium and its grains, including the geometry and mechanical properties, are reported in table 1. In single-phase flow simulations, water was injected with constant velocity ($V_i = 5 \times 10^{-6}$ m/s) from the inlet, and a specific pressure was imposed to the outlet. Reynolds number (Re) was lower than 0.1 through the medium in all the simulations, so the fluid flow was laminar. As described in sect. 2, the grain's surfaces had no-slip boundary conditions for the flow equations On the lateral sides of the medium (the top and the bottom in fig. 2), symmetry boundary condition was implemented for the flow equations and fixed constraint boundary condition was applied for the grain's deformation equations. The spring constant ($\boldsymbol{k}$) value of 1 mN m^{-1} was considered for each grain to avoid their free movement. Although this value has not yet been studied experimentally; however, the target of avoiding the free movement of the grains could be fulfilled. Hence, the studied case could be a representative of a real condition in a reservoir.

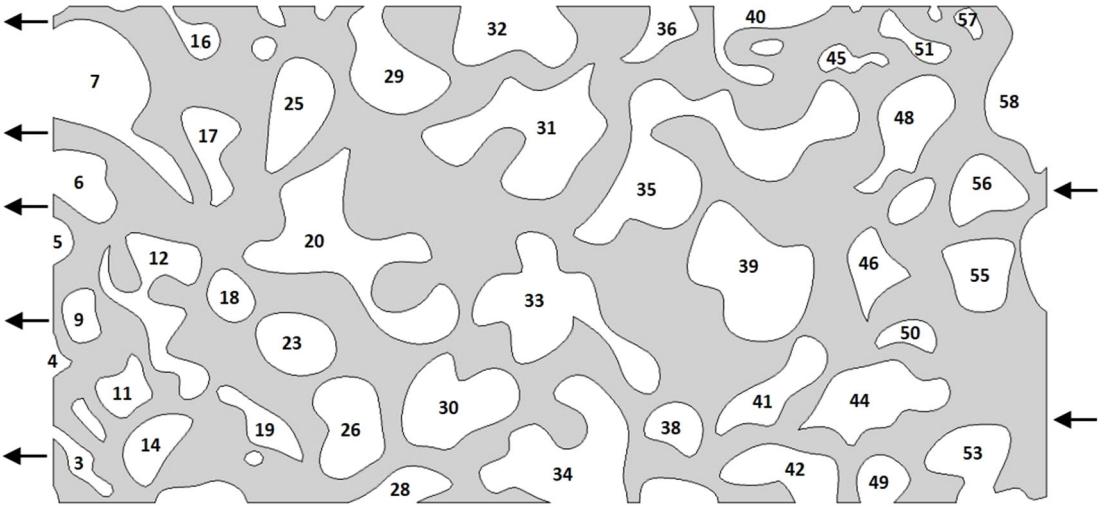

Fig. 2. The geometry of the studied real patterned porous medium [66] in which the grains' numbers and the inlet/outlet boundaries are specified.

Table 1. The properties of the simulated porous medium and its grains.

Medium length (μm)	640
Medium width (μm)	320
Average grain's diameter (μm) D_g	50
Density of solid grains (kg m^{-3})	2700
Solid grain's Young's modulus (MPa)	2500
Solid grain's Poisson's ratio	0.2

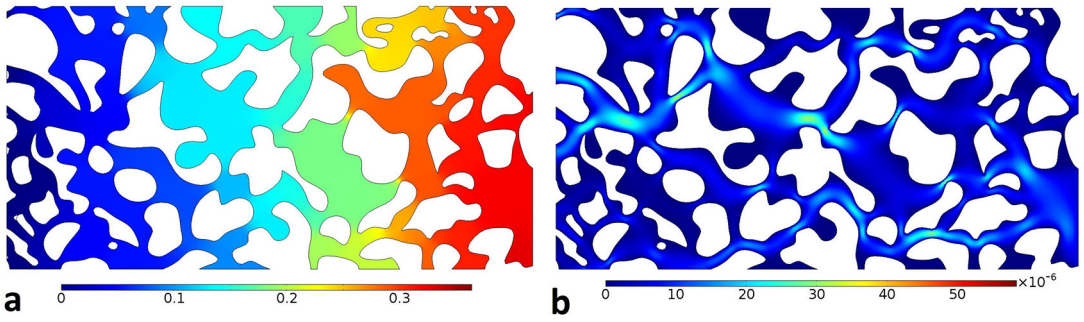

Fig. 3. (a) Pressure profile (Pa) and (b) velocity profile (m/s) of the base case model.

The pressure and velocity profiles of the base case, with zero pressure at the outlet and without grains' deformation and movement, is shown in fig. 3. As shown in fig. 3(a), a pressure gradient with the maximum of almost 0.35 Pa (in the outlet) happened in the medium due to the single-phase fluid flow. Velocity profile (fig. 3(b)) illustrates the main paths of the flow, with maximum of about 40×10^{-6} m/s, resulted by the pore/throat distribution in the base case. As expected, in each vertical cross section of the medium, the regions with lower flow velocity showed higher pressure, and vice versa.

In this section different single-phase flow cases were studied, summarized in table 2. The effects of deformations and movements of the medium grains as well as variations of the flow parameters, including pressure and fluid viscosity, were examined.

In fig. 4, the flow velocity profile inside the porous medium is compared for the first three cases 1a, 2a and 3a, in which all the flow properties are similar but the grain's mechanical boundary conditions are different. In case 1a, which has a rigid (non-deformable) medium, the relative maximum velocity in the medium ($V_{rm} = V_{max}/V_i$) was 7.35. The concentration of the flow streamlines was mostly present between the grains number 20-25, 31-33 and 41-42 (fig. 4,

Table 2. Different cases studied in the simulated single-phase flow model.

Case	Outlet pressure (MPa)	Grain's deformation	Grain's movement/rotation (unconsolidated)
1a	50		
2a	50	•	
3a	50	•	•
4a	20	•	
5a	20	•	•
6a	0	•	•

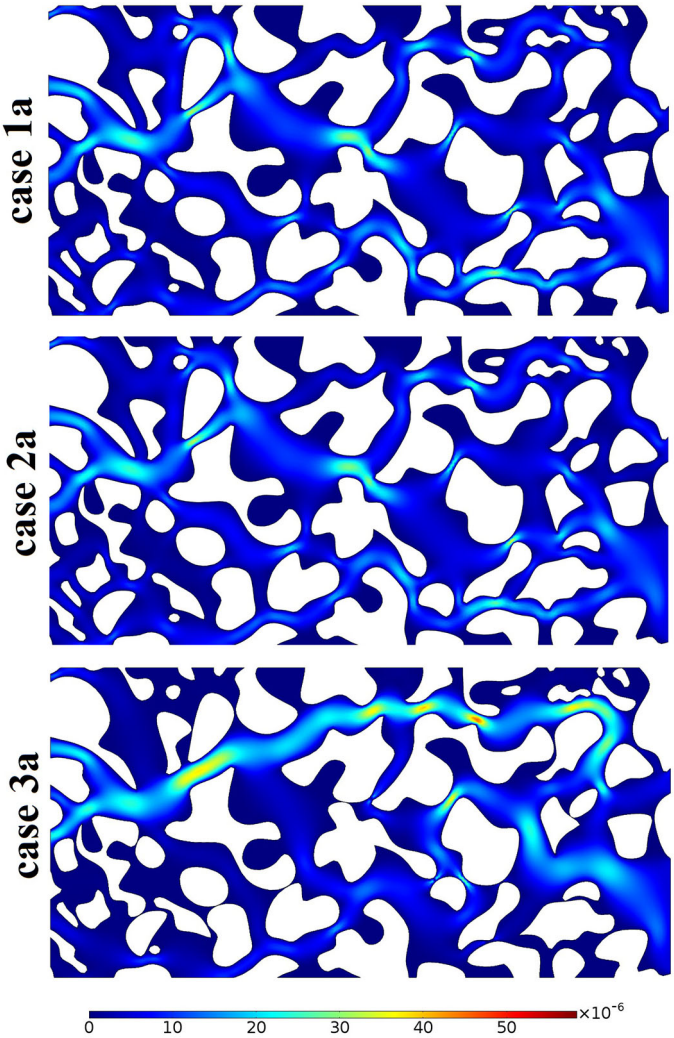

Fig. 4. Velocity profiles in the simulated single-phase porous medium for the studied cases 1a, 2a and 3a.

case 1a). In case 2a, on the other hand, the grains were deformed due to the fluid pressure, but not moved. V_{rm} in the medium of case 2a was 7.05, almost 4% lower than the first case, due to its larger pores and throats. However, as shown in fig. 4, the general velocity profiles, including the positions of the velocity peaks, were identical for the two cases. In case 3a, the grains not only were deformed by the medium pressure but also moved as a result of the flow drag. As depicted in fig. 4, the velocity magnitudes and distribution were totally changed from those of the former cases. V_{rm} increased to 9.1 in case 3a, almost 24% higher than case 1a. As a result of the grain's displacements and deformations, the flow streamlines were less evenly distributed in the medium, compared to the previous cases. For example, the grains number 31, 33 and 35 approached together, due to the imposed flow drag, so the main flow path was relocated

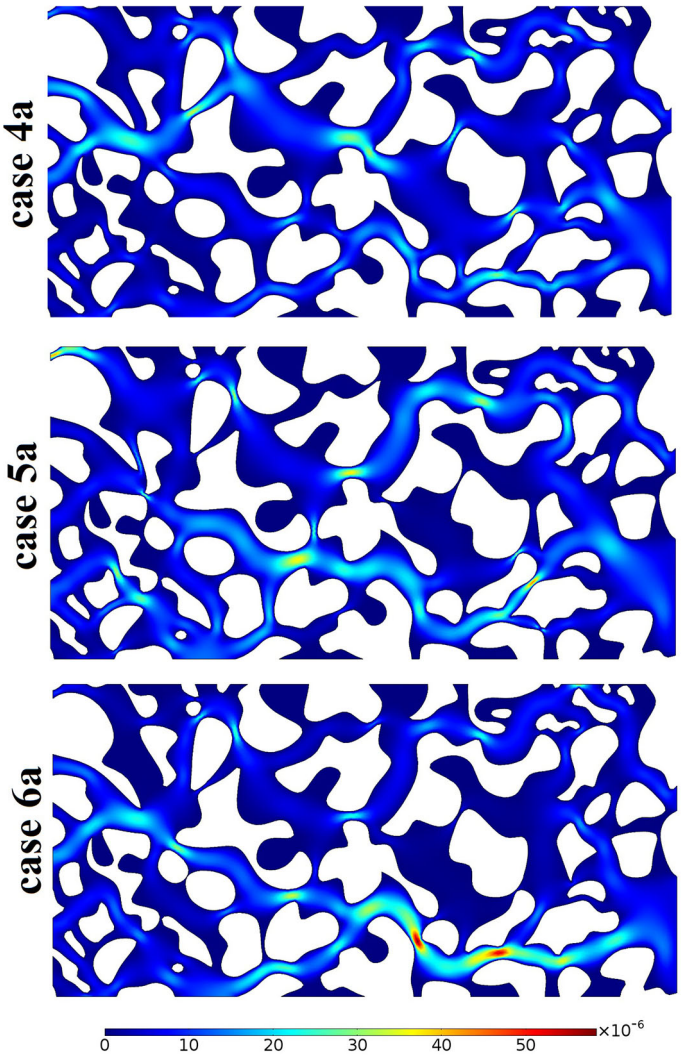

Fig. 5. Velocity profiles in the simulated single-phase porous medium for the studied cases 4a, 5a and 6a.

from the middle (between the grains 31 and 33) to the top (between the grains 31-32, 35-36-40 and 48-51). Also, the grains 41 and 42 approached together and banned one of the main flow paths at the bottom. As shown in fig. 4 for case 3a, both grain's movement and rotation happened. The most rotated grain (around 20° counterclockwise) was 33, which is located at the middle and has an arm in its shape. The drag force of the flow behind this arm caused such a rotation. Furthermore, the most displaced grain (almost 30 μm upward) was 33, which is relatively small and has more space around for movement.

Figure 5 presents the fluid flow velocity profile inside the medium in cases 4a, 5a and 6a (see table 2). The medium/fluid conditions in cases 4a and 5a are the same as those in cases 2a and 3a, respectively; however, the outlet pressure in these cases was reduced to 20 MPa. Although the velocity distribution profile in case 4a is quite identical with that of case 2a, its maximum velocity is 2.3% higher. Because of medium pressure effect, the throats and pores are relatively narrower in case 4a, compared to case 2a.

In case 5a, the grain deformation as well as their movement was taken into account (similar to case 3a), while the medium pressure was 20 MPa (similar to case 4a). As shown in fig. 5, not only the velocity magnitude but also the velocity profile of case 5a were totally different from those of cases 4a and 3a. V_{rm} of case 5a was 8.85, 23% higher than case 4a and 3% less than case 3a. Although case 5a had less grain compaction (so it was expected to have relatively thinner throats) compared to case 3a, its maximum velocity and streamline concentrated regions were less than case 3a. This is due to the influence of the grain displacement and rotation, which damped the grain deformation effect. The streamlines were mostly concentrated between the grains 20-30, 31-33, 35-40 and 41-44 in case 5a (fig. 5). The grains 20-25 and 31-32 were almost stuck together, so the flow path was fully different from that of cases 3a and 4a. The most rotated and displaced grain in case 5a, compared to case 4a, was 17, with approximately 15° clockwise rotation and 10 μm downward displacement.

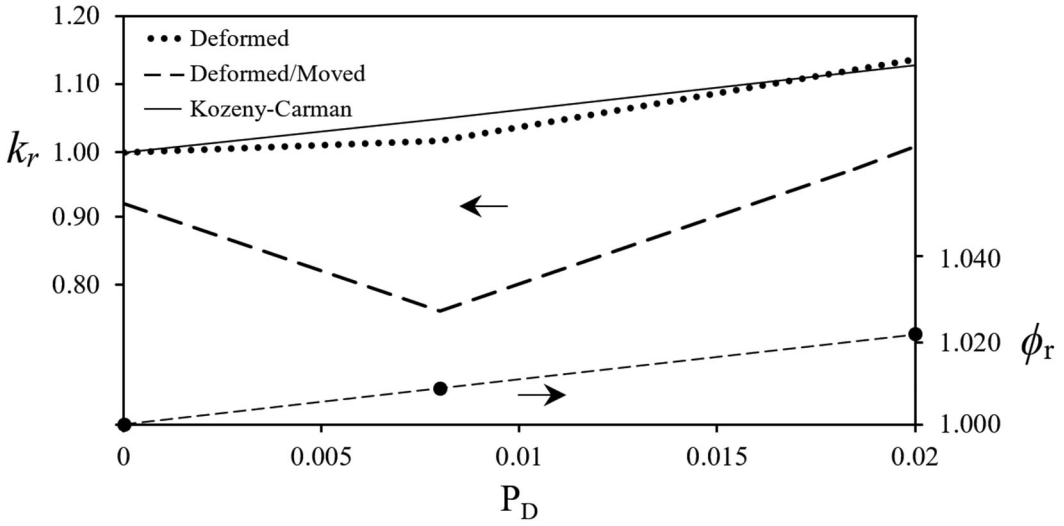

Fig. 6. Variation of the porosity ratio and permeability ratio *versus* dimensionless pressure. The permeability ratio was compared for the two studied cases with the grains' deformation and both deformation and movement/rotation. The permeability ratio predicted by Kozeny-Carman relation was included for comparison.

In case 6a, the outlet pressure was 0 MPa (similar to the base case), and deformation and movement of the grains were implemented. According to the simulation results, V_{rm} was 11.7, 32.1% higher than case 5a, and it is the maximum value among the studied cases. The regions between the grains 18-20, 20-30, 33-34, 34-38, 41-42 and 44-49 tolerated the most concentrated flow streamlines. Due to zero outlet pressure, the grains deformation was negligible, so the throats were narrower in this case, compared to the other studied case (1a to 5a). In the absence of grain's deformation, a pure grain displacement and rotation were happened in this case. The most displaced grain was again 17, with upward movement. The grain rotation was not considerable in this case.

As induced from fig. 4 and fig. 5 and the related discussions, the fluid pressure had a direct effect on the grain's compaction. Therefore, it is expected that the medium porosity and permeability would be modified by changing the fluid pressure. Figure 6 illustrates the changes in the medium porosity and permeability as a function of the fluid dimensionless pressure (p_D). Porosity ratio (ϕ_r) and permeability ratio (k_r) are defined here as the ratio of the porosity and permeability to those of the base case, with zero outlet pressure and without grains' deformation and movement. It was observed that the medium porosity is a function of the grains' compaction, and is independent of the grains' movement/rotation. As expected, within the studied range of the fluid pressure, variation of the medium porosity was linear with pressure. A 2% increase in p_D (*i.e.*, increasing pressure from 0 to 50 MPa) resulted in an almost 2% increase in the medium porosity. Also, at zero outlet pressure ($p_D = 0$), the medium porosity was identical to the base case.

As depicted in fig. 6, permeability was affected by the grain's mechanical boundary condition. For the medium in which the grains were just deformed, the permeability variation experienced approximately a linear trend. However, the gradient of k_r variation was slightly lower up to $p_D = 0.008$, then increased. By 2% increasing p_D, k_r varied from 1 to 1.13 (13% increase). The compaction of the grains increased the medium porosity, hence absolute permeability. The trend of k_r variation in this case (deformed grains without movement) was in a good agreement with the predicted one by Kozeny-Carman empirical formulation [67], which relates the permeability to the medium porosity and the average grain's diameter. This correlation can be stated as $k_{abs} = CD_g^2\varphi^3/(1-\varphi)^2$, where k_{abs} is the absolute permeability of the medium, D_g is the average grain's diameter, φ is the porosity of the medium and C is the Kozeny-Carman constant the depends on the type of porous medium.

However, considering both grains' deformation and movement/rotation (assuming unconsolidated medium) changed the behavior of the permeability variation *versus* pressure (fig. 6). In the case of the medium with deformable and moveable grains, the initial k_r (at $p_D = 0$) was 0.92 (compared to the base case). This lower permeability (compared to the base case) revealed the influence of displacement and rotation of the grains. Furthermore, by increasing p_D up to 0.008, although the medium porosity increased, k_r lowered to less than 0.08 (almost 15% reduction). Then, by increasing the pressure (up to $p_D = 0.02$) it was increased to almost 1. So, in unconsolidated media, the prediction of the medium permeability could be challenging; where the grain's unpredictable positions and directions are affected by the imposed fluid pressure.

Figures 7 and 8 reveal the influence of the medium flow Re on the velocity profile and permeability ratio, respectively. Re was modified here in the range of 0.0005 to 0.005 by modification of the injection velocity and (or) the fluid viscosity. In the studied cases, both deformation and movement/rotation were included and the pressure in the

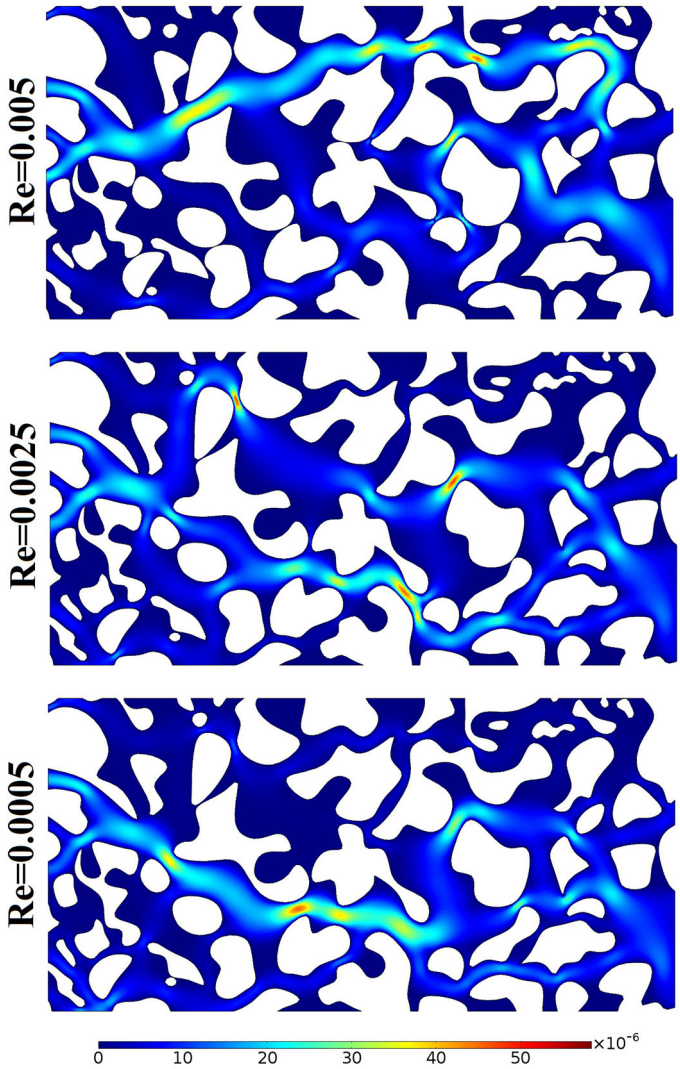

Fig. 7. Velocity profiles in the simulated single-phase porous medium for the studied cases under different Reynolds number.

outlet was set to 50 MPa. As shown in fig. 7, the velocity distribution in the unconsolidated medium is a function of the flow Re. The case with $Re = 0.005$ is case 3a, which was previously described. As Re decreased to 0.0025, V_{rm} was increased to 9.66 (almost 6% higher than the case of $Re = 0.005$). The regions between the grains 25-29, 30-33, 33-34, and 35-39 were the paths for the majority of the streamlines, completely different from case 3a. By further reduction of Re to 0.0005, V_{rm} was decreased to 9.1 (almost identical to case 3a with $Re = 0.005$). So, in these studied cases, by decreasing Re (decreasing injection velocity or increasing fluid viscosity), the velocity peak in the medium increased and then again decreased, due to new allocations of the medium grains. In this case, the streamlines were concentrated in the regions between the grains 18-20, 20-30, 30-33, and 33-34 different from the previous cases with higher Re. General comparison of the grains' distribution profiles in fig. 7 shows that as Re increased, the grains in the lower half of the medium were more tightened and those on the upper half were loosed; so, the flow streamlines transferred to the upper parts of the medium. As a result of this phenomenon, the main flow stream in the case with $Re = 0.005$ went along the single path at the top of the medium.

Figure 8 illustrates the variation of the medium permeability ratio (k_r) as a function of the reciprocal of Re. It is observed that, generally, the medium absolute permeability increased by reducing Re (increasing Re^{-1}). The gradient of k_r variations was increased by Re^{-1} in almost a parabolic trend. 10 times decreasing Re (from 0.005 to 0.0005), resulted in more than 35% increase in the medium absolute permeability. The new allocation of the grains by Re modification (observed in fig. 7) would result in such an observation.

3.3 Two-phase flow models

The same medium, as described in sect. 3.2, was considered for two-phase displacement simulations. The properties of the medium grains and boundary conditions are similar to the single-phase flow model. The medium was initially

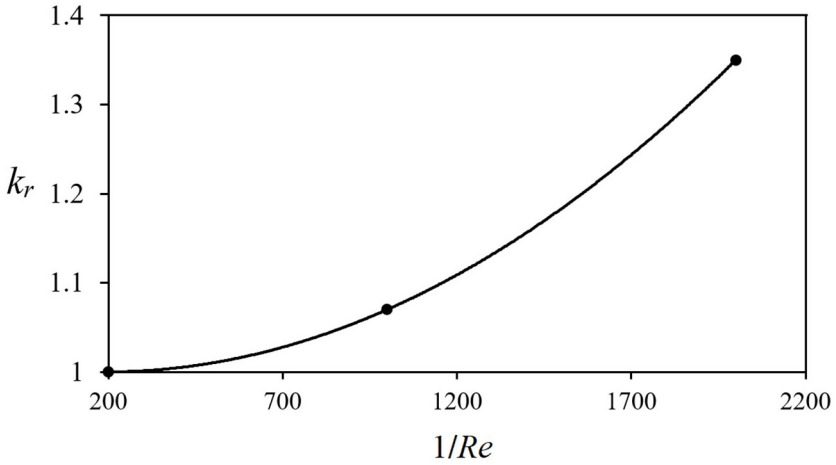

Fig. 8. Permeability ratio as a function of the reversed Reynolds number in the simulated single-phase flow model.

Table 3. Different cases studied in the simulated two-phase flow model.

Case	Contact angle°	Deformation	Movement
1b	60		
2b	60	•	
3b	60	•	•
4b	90		
5b	90	•	
6b	90	•	•
7b	120		
8b	120	•	
9b	120	•	•

saturated with the oil phase ($\mu_o = 0.006\,\text{Pa.s}$ and $\rho_o = 800\,\text{kg m}^{-3}$), displaced by the water phase, injected with constant velocity ($V_i = 5 \times 10^{-4}\,\text{m/s}$). Re in all the simulations was less than 0.1, so the flow was laminar. Pressure in the outlet boundary was set to 50 MPa. The boundary condition for the medium grains' surface was wetted wall at specific contact angle (see sect. 2.1). Similar to the single-phase sensitivity studies, two-phase fluid flow simulations were done here by considering the grains' deformation with/without movement/rotation. However, the grains' contact angle was the main studied parameter. Table 3 summarizes different studied cases in this section.

The capillary number and viscosity ratio are defined as $Ca = \mu_w V_i/\sigma$ and $M = \mu_w/\mu_o$, respectively. These parameters, together, determine the type of the flow instabilities in the absence of the gravity force [7]. In all the simulated models, the displacement profile became unchanged at a specific time after water breakthrough, which is called here stabilized fluid distribution.

Figure 9 compares the fluid distribution profiles and velocity fields in cases 1b, 2b, and 3b, in which the grains' contact angle was 60° (water-wet medium), while the grains' mechanical boundary conditions were different. In the studied cases $\log Ca = -4.7$ and $\log M = -0.8$. The dark blue and red colors represent water and oil phases, respectively, and the color gradient shows the mixing zone of the interface. As shown in fig. 9, compaction of the grains (case 2b) did not change the phase distribution, compared to the case with rigid medium (case 1b). In both media, water progressed almost piston-like up to the middle of the medium, then became unstable and formed a thick finger with large trapped volumes of oil in the bottom-right and top-left corners of the medium. According to the stability phase diagram presented by Rokhforouz *et al.* [12], Lenormand *et al.* [68] and Zhang *et al.* [69] the displacement regime (at the studied Ca and M) is in the crossover between viscous and capillary dominant flow. Comparing the fluid distributions of case 1b and 2b, it is observed that in response to only deformation of the grains, the path of water phase inside the porous medium was not changed. Also, the obtained velocity distributions were quite similar in these cases. The relative maximum velocity (V_{rm}) was almost identical for both media and was about 0.36. Case 3b, on the other hand, showed different displacement and velocity profiles. In this case, the grains' deformation and movement were simultaneously considered (see table 3). Although, the water progress profile up to the middle of the medium was stable (similar to cases 1b and 2b), the thickness of the formed finger in case 3b was larger than those in the

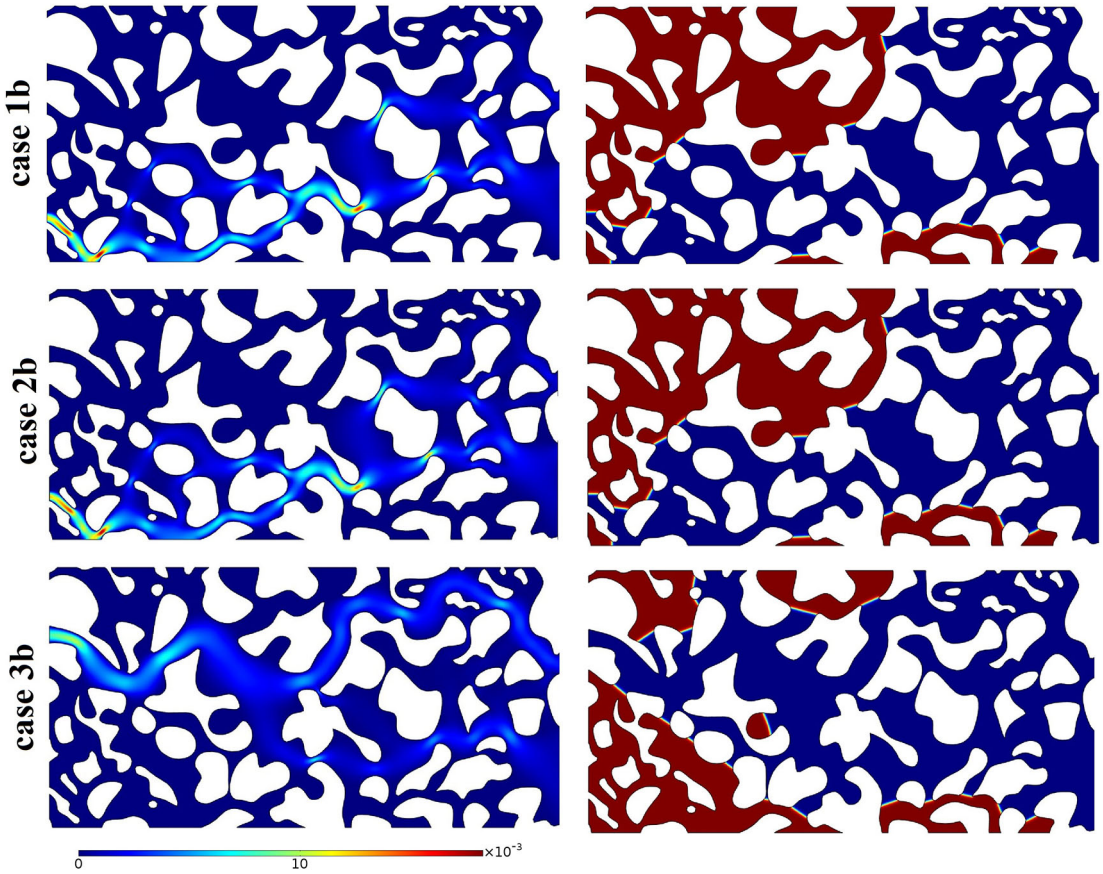

Fig. 9. The stabilized velocity and fluid distribution profiles in the simulated two-phase flow models at a contact angle of 60° (cases 1b, 2b and 3b).

former cases; hence, a relatively lower trapped-oil volume was predicted in this model. The main grains' movement in this case happened in the grains 26, 30 and 33. As a result of these medium modifications, the path of the water front movement was changed from the bottom (in cases 1b and 2b) to the top of the medium (in case 3b). The velocity was relatively more evenly distributed in case 3b, compared to the previous cases and V_{rm} was almost 20 in this case.

Figure 10 demonstrates the stabilized distribution of the fluids and velocity profiles in the models of cases 4b, 5b and 6b with the grains' contact angle of 90° (neutral wetting condition). The fluid displacement profile was quite similar in cases 4b (with rigid medium) and 5b (with grain compaction). It was unstable (including fingerings) with numerous small trapped-oil blobs in the middle of the medium. However, there was a small difference between the fluid profiles of the two models in a small region close to the grain 58. This small difference had not resulted in distinct velocity profiles for these two models. V_{rm} for cases 4b and 5b was 28.7 and 26.7, respectively. Case 6b (with grains' deformation and movement/rotation) showed completely different fluid profiles and velocity distribution compared to cases 4b and 5b, similar to what was observed for the water-wet media. The main movements and rotations were observed in the grains 33 and 56. As shown in fig. 10, in cases 4b and 5b, the main water streams went along a path below the grain 35; while for case 6b, since the grains 33, 35 and 39 approached to each other and the previous path was narrowed, a new water path was formed above the grain 35. So, the middle of the medium (all around the grain 39) remained unswept in case 6b. The number and morphology of the small trapped-oil volumes were also changed, compared to cases 4b and 5b. The velocity field of case 6b (fig. 10) also reveals this main water path. V_{rm} was 21 in this case, 5% higher than that of case 3b and 27% and 21% less than cases 4b and 5b.

Figure 11 illustrates the stabilized fluid and velocity distributions for the model with a contact angle of 120° (cases 7b, 8b and 9b in table 3). Cases 7b and 8b showed almost similar fluid profiles, except some differences around the grains number 46 and 55 (close to the inlet). In general, the displacement profile in both cases (oil-wet media) was unstable containing several fingerings, in agreement with the experimental observations [69–74]. The fingers were thinner than those in the previous cases (water wet and neutral wet models), one of those reached the outlet. Several small trapped-oil blobs were left between the fingers and large trapped-oil volumes remained unswept in the medium, especially on the top. The recovery factor was, expectedly, less than that of the previous cases; since it was a drainage process, in which the non-wetting phase displeased the wetting phase. The velocity profiles were also similar for cases

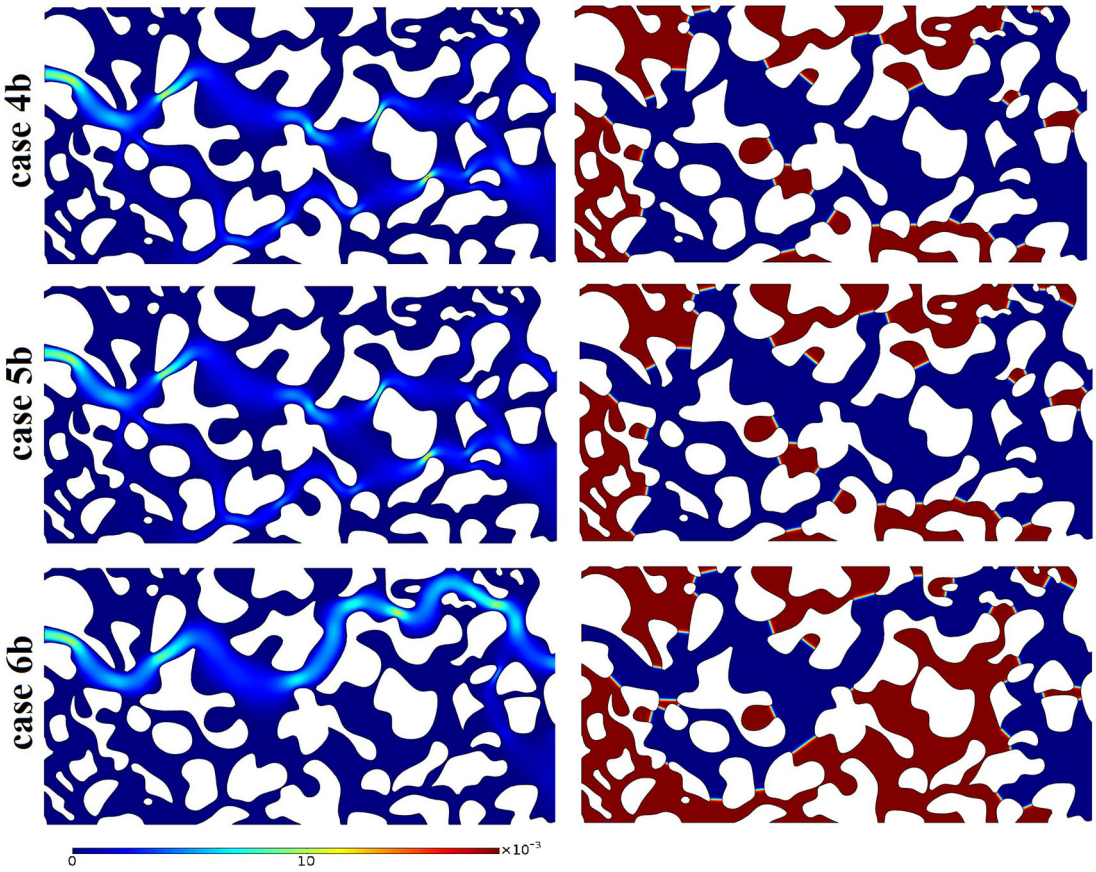

Fig. 10. The stabilized velocity and fluid distribution profiles in the simulated two-phase flow models at a contact angle of 90° (cases 4b, 5b and 6b).

7b and 8b, and V_{rm} was 32.1 and 29.7, respectively. On the other hand, case 9b, in which the grains were deformed and moved, resulted in a completely different fluid and velocity profile. It contained mainly a single advancing thin water finger with a thick branch at the middle. The breakthrough position of the water finger was not changed compared to cases 7b and 8b. In the bottom of the model in case 9b, the distance between the grains, for example 33 and 34, became less than that of cases 7b and 8b; hence, the path of the finger progress was on the top of the model, different from cases 7b and 8b. V_{rm} was 21, which was 35%, 29% lower than in cases 7b and 8b, respectively.

Figure 12 compares the stabilized water saturation, S_w, or oil recovery factor in other words, in the studied two-phase flow cases (cases 1b to 9b) as a function of the medium grains' contact angle. It is observed that S_w values for the rigid media (cases 1b, 4b and 7b) and those with only grains' compaction (cases 2b, 5b and 8b) were almost coincident at different contact angles. S_w was about 0.6 at $\theta = 60°$, then increased to 0.7 at neutral wetting condition ($\theta = 90°$), and as the medium became oil-wet, it was decreased to about 0.5 (at $\theta = 120°$). However, the media with both deformed and moved grains (cases 3b, 6b and 9b) showed completely different trend of S_w *versus* θ. In these cases, as the medium became more oil-wet (θ increased), the oil recovery factor (S_w) was decreased. S_w decreased from 0.7 to 0.4 as θ increased from 60° to 120°. The medium with deformable and moveable grains showed a higher oil recovery factor at water wet condition (case 3b), while a lower recovery factor at oil- and neutral-wetting conditions, compared to the two other cases. In other words, it had greater variations in S_w at different θ values.

Figure 13 depicts the water endpoint relative permeability values (the relative permeability of water at the stabilized saturation of water phase) for the different studied cases. The black, red and blue dots belong to contact angles of 60°, 90° and 120°. The relative permeability is one of the main parameters in two-phase flow problems in porous media, which indicates the ability of each phase to flow in the presence of the other phase. For water phase, it is obtained by the following equation [75]:

$$k_{rel}^{w} = \frac{Q_w \mu_w}{k_{abs} H \nabla p_w}, \tag{15}$$

where k_{abs} is the absolute permeability of the micro model domain and it can be calculated when only one phase, *e.g.* the water phase, flows through the medium. Q_w is the water flow rate in the medium and is obtained by integrating the

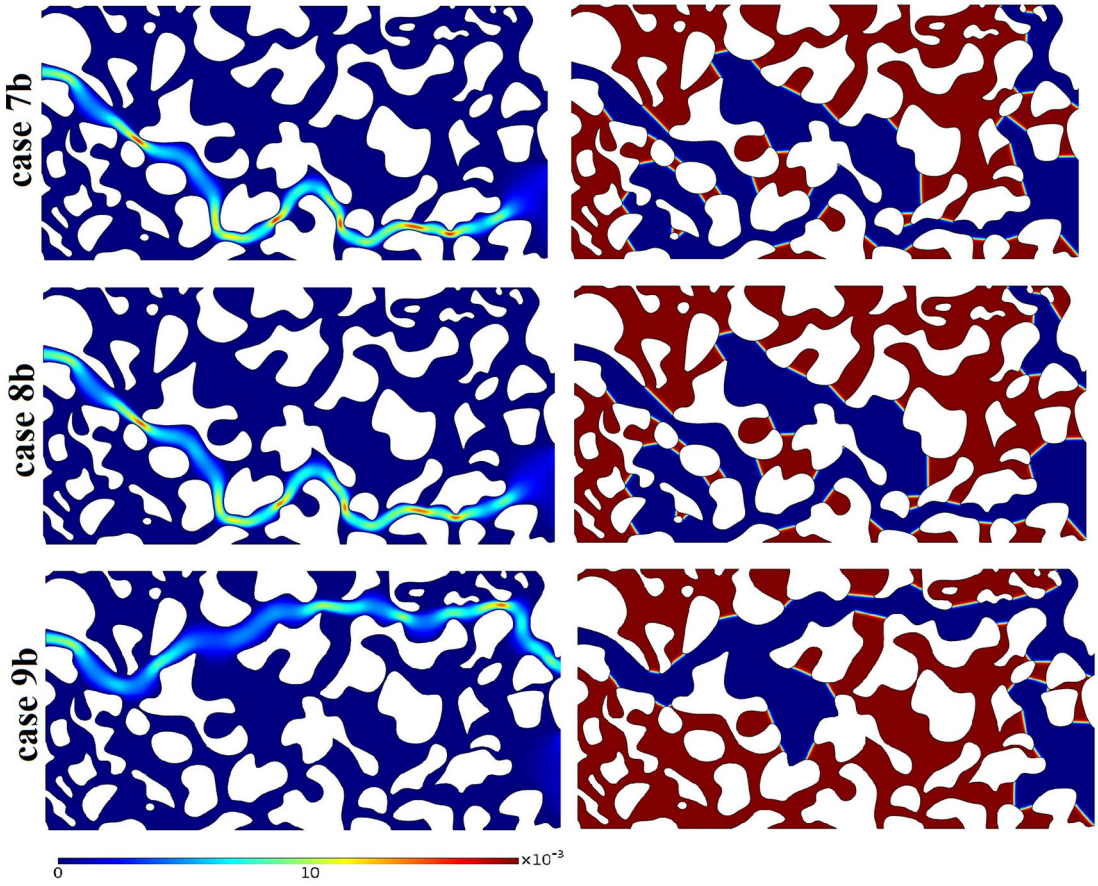

Fig. 11. The stabilized velocity and fluid distribution profiles in the simulated two-phase flow models at contact angle of 120° (cases 7b, 8b and 9b).

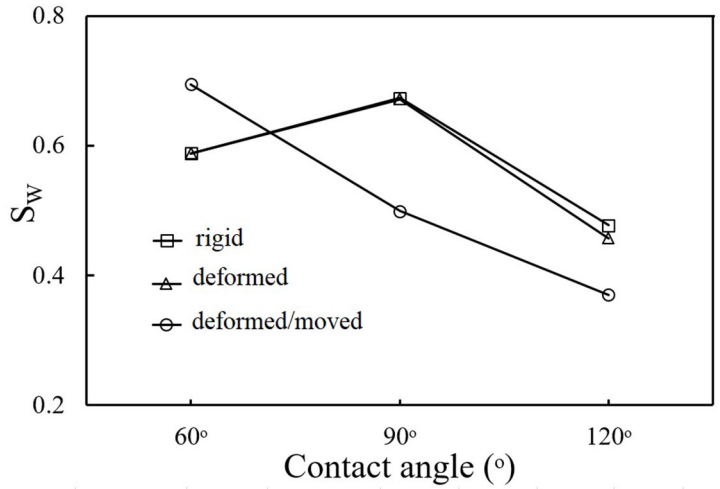

Fig. 12. The Stabilized water saturation (S_w) as a function of the grains' surface contact angle (θ) in different simulated two-phase flow models.

steady fluid velocity on the inlet. H is the width of the micro model and ∇p_w is the pressure gradient in the domain. As shown in fig. 13, k^w_{rel} varied between 0.74 to 0.89, and the related stabilized S_w variation range was between 0.37 and 0.69. In the rigid medium (triangular dots) and that with deformable grains (square dots), in general, k^w_{rel} decreased inversely with θ. In the medium with grains' deformation, as an instance, k^w_{rel} was 0.86 (at $S_w = 0.59$) for $\theta = 60°$; while, for $\theta = 90°$, k^w_{rel} decreased to 0.84 (at $S_w = 0.67$), despite the increase of S_w. By increasing θ above 90°, k^w_{rel} was further decreased, in accordance with S_w. However, in the case of medium with both grains' deformation and

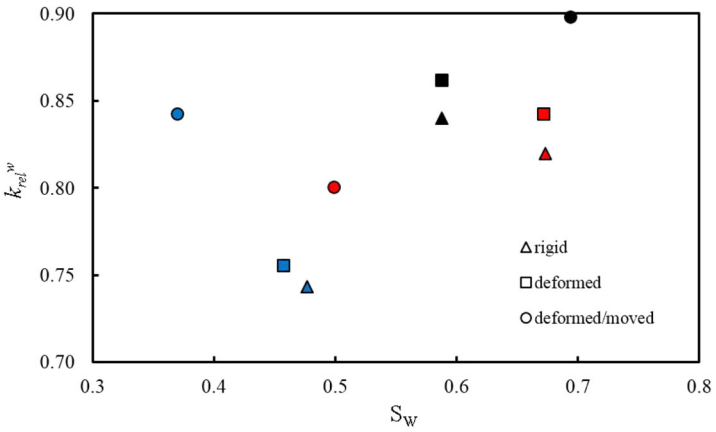

Fig. 13. Water relative permeability endpoints (k_{rel}^{w}) as a function of the water saturation (S_w) for media with different grains' contact angles of 60° (black), 90° (red) and 120° (blue) in the simulated two-phase flow cases.

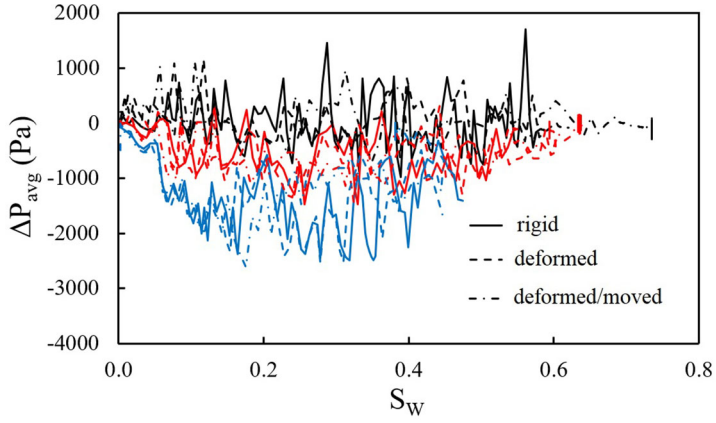

Fig. 14. The macro-scale averaged pressure (ΔP_{avg}) as a function of water saturation (S_w) at different grains' contact angles (black line: contact angle of 60°, red line: contact angle of 90°, blue line: contact angle of 120°).

movement (circular dots), there was not a regular trend in k_{rel}^{w} *versus* contact angle. In this case, the maximum k_{rel}^{w} (0.89) happened at the highest stabilized S_w (0.69) at $\theta = 60°$ (water-wet condition). By increasing θ to 90°, k_{rel}^{w} decreased to 0.80 (at S_w 0.5). Then k_{rel}^{w} increased again to 0.84 (at S_w 0.37), as $\theta = 120°$.

As shown in fig. 13, for the water-wet (black dots) and the oil-wet media (blue dots), the rigid medium had the minimum k_{rel}^{w}, and the one with both deformation and movement had the maximum k_{rel}^{w}. However, for water-wet medium, S_w increased with k_{rel}^{w}, while it is vice versa in the case of a oil-wet medium. For neutral-wet medium (red dots), on the other hand, k_{rel}^{w} was maximum for the case of the medium with deformation, and minimum for the one with both deformation and movement. The range of variation in S_w in the neutral wetting condition (0.5 to 0.67) was higher than that of the other wettabilities.

Capillary pressure, which is defined as the difference in the pressures of the non-wetting and wetting phase at the interface, is another important parameter during multiphase flow problems. To study the trend of capillary pressure variations in the media as a function of fluid saturations, the average pressure difference between the oil- and water-filled regions (macro-scale capillary pressure), Δp_{avg}, was obtained as

$$\Delta p_{avg} = p_o - p_w, \tag{16}$$

$$p_o = \frac{\int_V pV_{fo}\mathrm{d}V}{\int_V V_{fo}\mathrm{d}V}, \qquad P_w = \frac{\int_V pV_{fw}\mathrm{d}V}{\int_V V_{fw}\mathrm{d}V}, \tag{17}$$

where p_w and p_o denote water and oil fluids pressure, respectively, which were volumetrically integrated over the water- and oil-filled volumes. V_{fw} and V_{fo} are the volume fraction of the water and oil phases.

Figure 14 depicts Δp_{avg} as a function of the water saturation (S_w) at different grains' contact angles, for the different studied cases with different mechanical grains' boundary conditions. In general, the trend of Δp_{avg} *versus* water saturation had unsteady fluctuations, known as Haines Jumps, occurring when the non-wetting fluid passes from the

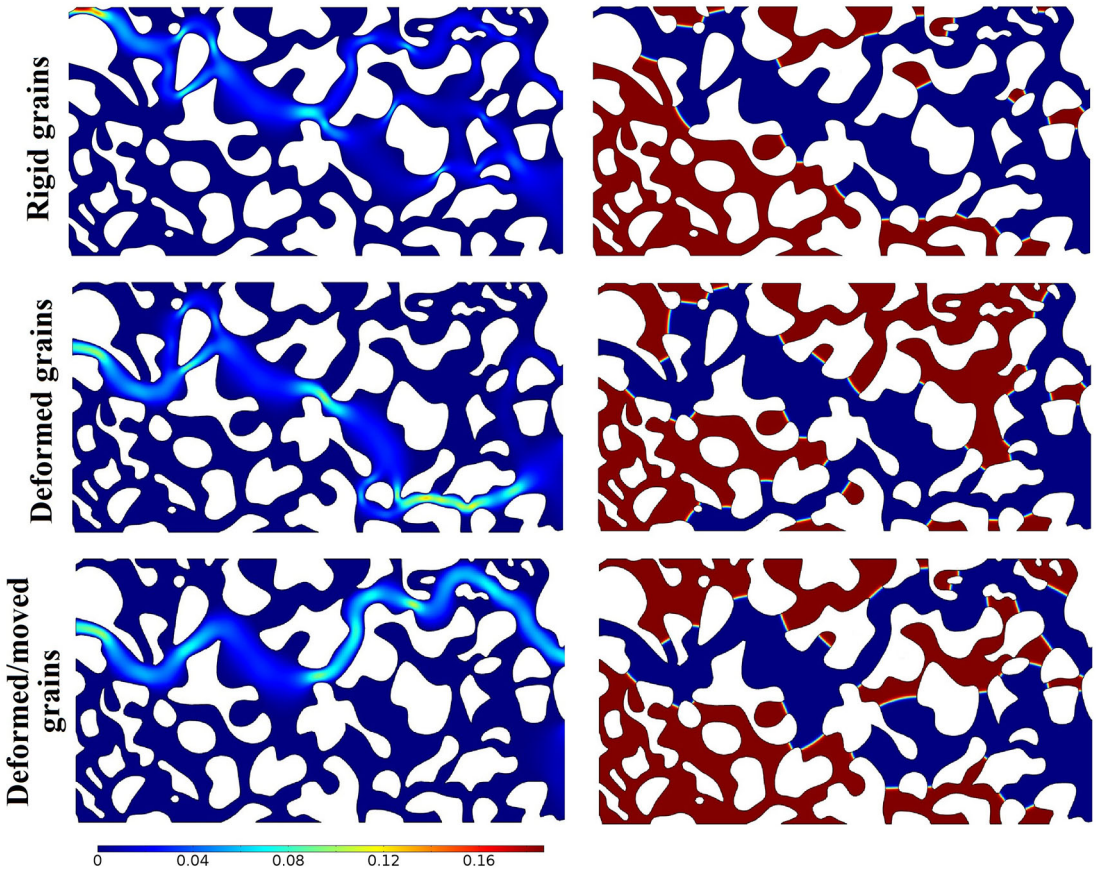

Fig. 15. Velocity profile and fluid distributions under contact angle of 90° conditions (flow regime changed).

pore neck into a wider pore body during the drainage process [76–78]. Once the invading fluid's pressure prevails the capillary entry pressure of a pore throat, the nearby pore body is filled rapidly [79]. As θ increased (the medium became more oil-wet), the sign of Δp_{avg} became more negative and its absolute value was increased. The negative sign in capillary pressures reveals the lower rate of imbibition process (at oil-wet conditions). A higher negative capillary pressure in the case of oil-wet media indicates flow resistance, resulting in lower sweep efficiency, as was observed in fig. 12. As shown in fig. 14, the positions and the sizes of the fluctuations depended on the grains' deformation and movements. At different wetting conditions, the biggest Δp_{avg} fluctuations were for the case of the rigid medium, while the one with deformation and movement showed the smallest fluctuations. This observation indicates that the grains were rearranged during displacement, in order to minimize the medium capillary pressure (flow resistance) at each fluid saturation.

The displacement regime in the flow through porous media mainly depends on M and Ca [12,68,69]. To address the effect of Ca on the interplay of fluid flow and grains' deformation/movements, the water injection velocity was increased to 5×10^{-3} m/s, so $\log Ca$ increased to -3.7. Figure 15 illustrates the stabilized distribution of the fluids and the related velocity profiles in the medium at a grains' contact angle of 90°, in which $\log Ca = -3.7$ and $\log M = -0.8$. The effect of the grains' mechanical boundary conditions was studied here, which can be compared to cases 4b, 5b and 6b (with $\log Ca = -4.7$). Although cases 4b and 5b (with $\log Ca = -4.7$) showed similar fluid and velocity profiles (see fig. 10), the displacement and velocity profiles in the rigid medium and the one with deformable grains at $\log Ca = -3.7$ were totally different. Compared to the lower Ca ($\log Ca = -4.7$, fig. 10), the thickness of the formed fingerings in the media at $\log Ca = -3.7$ was relatively smaller. This may somehow indicate the shift of the flow regime from capillary-dominant to viscous-dominant, as Ca increased. In the case with the rigid grains, despite the one with deformable grains, the water phase passed through the pores and throats between the grains number 31-35-36-40. The position of the water breakthrough was also different in the two models. Accordingly, the velocity distribution and the peak positions were different, especially around the grains 41-44 and also in the outlet. V_{rm} was 37.3 for the rigid medium (occurring close to the outlet), while it was 25.5 for the case with deformable grains (occuring close to the inlet).

As shown in fig. 15, the flow profile in the case with deformable/moveable grains was expectedly changed from the above-studied cases, and was comparable with that of case 6b (fig. 10), with some differences. The grains number 33, 35 and 39 approached to each other, so water passed through the path above the grain 35 and could not reach the outlet from the middle of the medium. The velocity distribution was quite similar to case 6b, and its V_{rm} was 21.3.

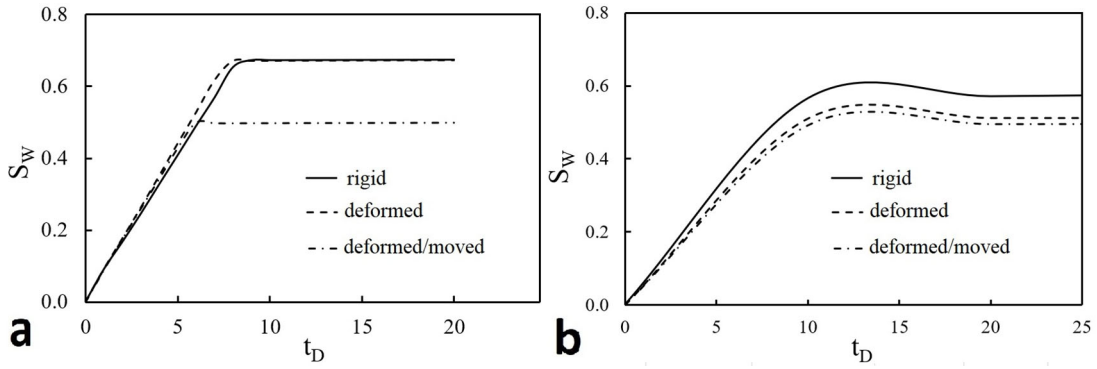

Fig. 16. Water saturation (S_w) as a function of dimensionless time (t_D) for different simulated cases at (a) $\log Ca = -4.7$ (b) and $\log Ca = -3.7$.

Figure 16 shows the water saturation (S_w) profile as a function of dimensionless time (t_D) for cases 4b, 5b and 6b at $\log Ca = -4.7$ (fig. 16(a)) compared to the corresponding cases at $\log Ca = -3.7$ (fig. 16(b)). As pointed out, all these cases had neutral wetting conditions ($\theta = 90°$). In general, S_w (oil recovery factor) *versus* t_D was highly affected by both Ca and the medium grain's mechanical boundary conditions. At the lower Ca (fig. 16(a)), the rigid medium (case 4b) and the one with only deformed grains (case 5b) showed almost identical behavior for S_w *versus* t_D. However, at the higher Ca (fig. 16(b)), the medium with deformed grains resulted in a lower ultimate recovery (about 7%) compared to the rigid medium. For the case of $\log Ca = -3.7$ (fig. 16(b)), the consideration of the grains' deformation and movement had not a significant effect on S_w; while, the case with $\log Ca = -4.7$ (fig. 16(a)) showed an opposite behavior. In the case of $\log Ca = -4.7$, the medium with only deformed grains resulted in a considerable (about 20%) higher ultimate S_w than the one with deformed/moved grains; while it was less than 3% for the case with $\log Ca = -3.7$. Also, at the higher Ca (fig. 16(b)), the rate of changes in S_w *versus* t_D before water breakthrough time was lowered as the grains' deformation and movement were taken into account. While, in the case of $\log Ca = -4.7$ (fig. 16(a)), this rate was slightly increased.

4 Conclusion

The constructed simulation model, *i.e.*, coupled Cahn-Hilliard phase field and Navier-Stokes equations as well as stress-strain equations and Arbitrary Lagrangian/Eulerian mesh alteration equations, was successfully validated with the analytical solution of a simple model, which was a single grain gone through single-phase flow. Then different sensitivity analyses were done on single two-phase flow in a consolidated/unconsolidated real-patterned micro-scale porous medium.

In the single-phase cases, the general velocity profiles, including the positions of the velocity peaks, were identical for the cases with rigid and deformable medium. As the grains' movement/rotation were taken into account, the velocity magnitudes and distribution were totally changed. It was observed that the variation of the medium porosity was linear with fluid pressure, and was independent of the grains' movement/rotation. Also, permeability was affected by the grain's mechanical boundary condition. For a medium in which the grains were just deformed, the permeability variation experienced approximately a linear trend and was in good agreement with the one predicted by Kozeny-Carman empirical formulation. However, considering both grains' deformation and movement/rotation changed the behavior of the permeability variation *versus* pressure, in an irregular manner. In the studied unconsolidated cases, by decreasing Re (decreasing injection velocity or increasing fluid viscosity), the medium absolute permeability was increased.

In the simulated two-phase (water-oil) models, also, compaction of the grains did not highly change the velocity and phase distribution at different medium contact angles. By considering simultaneous grains' deformation/movement, velocity and fluid displacement profiles were highly affected. It was observed that displacement efficiency (recovery factor) variation *versus* grains' contact angle was almost coincident for the rigid medium and that with only grains' compaction, with an irregular trend. However, the unconsolidated medium, *i.e.*, with both deformed and moved/rotated grains, showed a completely different regular (decreasing) trend in displacement efficiency as the medium became more oil-wet. The water relative permeability end-point decreased by the medium contact angle in the rigid medium and that with deformable grains. However, as the case grains' movement/rotation was taken into account (unconsolidated medium), this behavior was changed; as neutral wetting condition resulted in the least relative permeability end-point. The oil-wet medium was more affected by the geomechanical boundary condition, in terms of variations in the relative permeability. As the flow regime moved from viscous to capillary flow, *i.e.*, capillary number decreased, the effect of the medium geomechanical behavior (*e.g.*, the grains' movement/rotation) was more pronounced.

The qualitative and quantitative findings of this study shed light upon the importance of considering the geomechanical behavior of porous media on different flow problems. It helps the researcher in this field for more accurate prediction of the porous media responses to different displacement processes.

This research did not receive any specific grant from funding agencies in the public, commercial or not-for-profit sectors.

References

1. M. Muskat, *The Flow of Homogeneous Fluids through Porous Media* (McGraw-Hill, New York, 1982).
2. P. Lehmann, M. Berchtold, B. Ahrenholz, J. Tölke, A. Kaestner, M. Krafczyk, H. Flühler, H.R. Künsch, Adv. Water Resour. **9**, 31 (2008).
3. C. Cottin, H. Bodiguel, A. Colin, Phys. Rev. E **4**, 82 (2010).
4. B. Ahrenholz, J. Niessner, R. Helmig, M. Krafczyk, Water Resour. Res. **7**, 47 (2011).
5. H.A. Akhlaghi Amiri, A.A. Hamouda, Int. J. Multiphase Flow **52**, 22 (2013).
6. S. Berg, H. Ott, S.A. Klapp, A. Schwing, R. Neiteler, N. Brussee, A. Makurat, L. Leu, F. Enzmann, J.-O. Schwarz, M. Kersten, S. Irvine, M. Stampanoni, Proc. Natl. Acad. Sci. U.S.A. **10**, 110 (2013).
7. H.A. Akhlaghi Amiri, A.A. Hamouda, Int. J. Multiphase Flow **61**, 14 (2014).
8. K. Kitamura, F. Jiang, A.J. Valocchi, S. Chiyonobu, T. Tsuji, K.T. Christensen, JGR Solid Earth **119**, 7564 (2014).
9. A. Setiawan, T. Suekane, Y. Deguchi, K. Kusano, J. Flow Control, Meas. & Visual. **2**, 25 (2014).
10. T. Tsuji, F. Jiang, K.T. Christensen, Adv. Water Resour. **95**, 3 (2016).
11. F. Basirat, Z. Yang, A. Niemi, Adv. Water Resour. **109**, 181 (2017).
12. M.R. Rokhforouz, H.A. Akhlaghi Amiri, Adv. Water Resour. **113**, 260 (2018).
13. V.H. Nguyen, A.P. Sheppard, M.A. Knackstedt, W. Val Pinczewski, J. Petrol. Sci. Eng. **1**, 52 (2006).
14. R.I. Al-Raoush, Environ. Sci. Technol. **13**, 43 (2009).
15. D. Wildenschild, R.T. Armstrong, A.L. Herring, I.M. Young, J. William Carey, Energy Proc. **4**, 4945 (2011).
16. F. Jiang, T. Tsuji, C. Hu, Transp. Porous Media **1**, 104 (2014).
17. J.G.I. Hellström, V. Frishfelds, T.S. Lundström, J. Fluid Mech. **664**, 220 (2010).
18. M. Prodanović, J.T. Holder, S.L. Bryant, Int. J. Oil, Gas Coal Technol. **2-3**, 5 (2012).
19. D.R. Hewitt, J.S. Nijjer, M.G. Worster, J.A. Neufeld, Phys. Rev. E **2**, 93 (2016).
20. A. Settari, D.A. Walters, SPE J. **6** (2001) `https://doi.org/10.2118/74142-PA`.
21. L.K. Thomas, L.Y. Chin, R.G. Pierson, J.E. Sylte, SPE J. **8** (2003) `https://doi.org/10.2118/87339-PA`.
22. R.H. Dean, X. Gai, C.M. Stone, S.E. Minkoff, SPE J. **11**, 132 (2006).
23. J. Kim, H.A. Tchelepi, R. Juanes, SPE J. **18** (2013) `https://doi.org/10.2118/141268-PA`.
24. Q.J. Zhu, Y.F. He, Y. Yin, Mater. Res. Innov. **18**, 22 (2014).
25. F.O. Alpak, SPE J. **20**, 1366 (2015).
26. F. Doster, J.M. Nordbotten, in *Proceedings of the SPE Reservoir Simulation Symposium, Texas, USA, 2015*, Vol. **10** (2015).
27. A. Wilson, J. Petrol. Technol. (2015) `https://doi.org/10.2118/1115-0078-JPT`.
28. A. Gajo, F. Cecinato, B. Loret, Transp. Porous Med. **1**, 116 (2017).
29. P. Samier, *Proceedings of the SPE Reservoir Simulation Conference, Texas, USA, 2017*, Vol. **7** (2017).
30. G.U. Grün, H. Wallner, H.J. Neugebauer, Geolog. Rund. **1**, 78 (1989).
31. L. Xikui, Commun. Appl. Numer. Methods **2**, 6 (1990).
32. L. Xikui, O.C. Zienkiewicz, Comp. Struct. **2**, 45 (1992).
33. N.A. Rahman, R.W. Lewis, Comp. Geotech. **1**, 24 (1999).
34. J.A. White, R.I. Borja, J.T. Fredrich, Acta Geotech. **4**, 1 (2006).
35. J.A. White, R.I. Borja, in *Proceedings of the ASME International Mechanical Engineering Congress and Exposition, United States, 2009*, Vol. **12** (2009).
36. H. Fatahi, M.M. Hossain, J. Petrol. Explor. Product. Technol. **2**, 6 (2016).
37. D.F. Boutt, B.K. Cook, J.R. Williams, Int. J. Numer. Anal. Methods Geomech. **9**, 35 (2011).
38. S. Bakhshian, M. Sahimi, Phys. Rev. E **4**, 94 (2016).
39. Y. Pan, R.N. Horne, Transp. Porous Med. **1**, 45 (2001).
40. Y. Pan, R.N. Horne, Transp. Porous Med. **2**, 45 (2001).
41. J.W. Both, K. Kumar, J.M. Nordbotten, F.A. Radu, in *Proceedings of the 6th Biot Conference on Poromechanics, Princeton, United States, 2017*, Vol. **5** (2017).
42. J.L. Auriault, O. Lebaigue, G. Bonnet, Transp. Porous Med. **2**, 4 (1989).
43. B. Ju, Y. Wu, T. Fan, J. Petrol. Sci. Eng. **3-4**, 76 (2011).
44. A. Settari, F.M. Mourits, SPE J. (1998) `https://doi.org/10.2118/50939-PA`.
45. R.H. Dean, X. Gai, C.M. Stone, S.E. Minkoff, SPE J. **1**, 11 (2006).
46. J. Zhao, T. Shan, Powder Technol. **239**, 248 (2013).

47. L. Jin, M.D. Zoback, JGR Solid Earth **122**, 7626 (2017).
48. V.A. Torrealba, Z.T. Karpyn, H. Yoon, K.A. Klise, D. Crandall, Geofluids **1**, 16 (2016).
49. Y. Kaneko, O. Sano, Phys. Fluids **3**, 17 (2005).
50. J.I. Siddique, D.M. Anderson, A. Bondarev, Phys. Fluids **1**, 21 (2009).
51. M. Chekired, V. Roubtsova, in *Proceedings of the Geotechnical Special Publication, Canada, 2010*, Vol. **2** (2010).
52. J.W. Cahn, J.E. Hilliard, J. Chem. Phys. **2**, 28 (1958).
53. P. Yue, C. Zhou, J.J. Feng, C.F. Ollivier-Gooch, H.H. Hu, J. Comput. Phys. **1**, 219 (2006).
54. C. Zhou, P. Yue, J.J. Feng, C.F. Ollivier-Gooch, H.H. Hu, J. Comput. Phys. **2**, 229 (2010).
55. D. Jacqmin, J. Comput. Phys. **1**, 155 (1999).
56. V. Badalassi, H. Ceniceros, S. Banerjee, J. Comput. Phys. **2**, 190 (2003).
57. F. Fichot, P. Meekunnasombat, J. Belloni, F. Duval, A. Garcia, M. Quintard, Nucl. Eng. Design **15**, 237 (2007).
58. A. Sommerfeld, *Lectures on Theoretical Physics: Mechanics of Deformable Bodies* (Academic Press, 1964).
59. R.O. Davis, A.P. Selvadurai, *Plasticity and Geomechanics* (Cambridge University Press, 2005).
60. R.B. Bird, W.E. Stewart, E.N. Lightfoot, *Transport Phenomena* (Wiley, 2009).
61. *COMSOL Multiphysics*, User's Guide, Version 4.4. (Comsol Inc., 2013).
62. S. Liang, J.Y. Yin, S.F. Xue, J. Canad. Petrol. Technol. **4**, 48 (2009).
63. T.J. Hughes, W.K. Liu, T.K. Zimmermann, Comp. Methods Appl. Mech. Eng. **3**, 29 (1981).
64. T. Liu, Q. Li, C. Zhao, Sci. China Phys., Mech. Astron. **4**, 56 (2013).
65. M. Rokhforouz, H. Akhlaghi Amiri, Phys. Fluids **6**, 29 (2017).
66. A.A. Keller, M.J. Blunt, A.P.V. Roberts, Transp. Porous Med. **3**, 26 (1997).
67. G.V. Chilingar, R. Main, A. Sinnokrot, J. Sedime. Res. **3**, 33 (1963).
68. R. Lenormand, E. Touboul, C. Zarcone, J. Fluid Mech. **189**, 165 (1988).
69. C. Zhang, M. Oostrom, T.W. Wietsma, J.W. Grate, M.G. Warner, Energy Fuels **8**, 25 (2011).
70. G. Løvoll, Y. Méheust, K.J. Måløy, E. Aker, J. Schmittbuhl, Energy **6**, 30 (2005).
71. D. Loggia, Z. Bo, L. Xiaorong, G. Vasseur, Transp. Porous Med. **1**, 80 (2009).
72. K.J. DeHoff, M. Oostrom, C. Zhang, J.W. Grate, Vadose Zone J. **4**, 11 (2012).
73. J. Sharma, S.B. Inwood, A. Kovscek, SPE J. **04**, 17 (2012).
74. Y. Teng, Y. Liu, L. Jiang, Y. Song, J. Zhao, Y. Zhang, D. Wang, Magn. Res. Imaging **7**, 34 (2016).
75. L.P. Dake, *Fundamentals of Reservoir Engineering* (Elsevier New York, 1978).
76. S. Berg, H. Ott, S.A. Klapp, A. Schwing, R. Neiteler, N. Brussee, A. Makurat, L. Leu, F. Enzmann, J.-O. Schwarz, M. Kersten, S. Irvine, M. Stampanoni, Proc. Natl. Acad. Sci. U.S.A. **110**, 3755 (2013).
77. R.T. Armstrong, N. Evseev, D. Koroteev, S. Berg, Adv. Water Resour. **77**, 57 (2015).
78. M.R. Rokhforouz, H.A. Akhlaghi Amiri, Adv. Water Resour. **124**, 84 (2019).
79. M.R. Rokhforouz, H.A. Akhlaghi Amiri, *Pore-level influence of wettability on counter-current spontaneous imbibition*, in *79th EAGE Conference and Exhibition, Paris, France* (2017) `https://doi.org/10.3997/2214-4609.201701510`.